1 **The effects of different footprint sizes and cloud algorithms on the**

2 **top-of-atmosphere radiative flux calculation from CERES**

3 **instrument on Suomi-NPP**

4 WENYING SU, *

Science Directorate, NASA Langley Research Center, Hampton, Virginia

5 LUSHENG LIANG, WALTER F. MILLER, VICTOR E. SOTHCOTT

Science Systems & Applications, Inc., Hampton, Virginia

Corresponding author address: Wenying Su, MS420, NASA Langley Research Center, Hampton, VA 23681.

E-mail: Wenying.Su-1@nasa.gov

6   ABSTRACT

7   Only one CERES instrument is onboard the Suomi-NPP and it has been placed in cross-

8   track mode since launch, it is thus not possible to construct a set of angular distribution

9   models (ADMs) specific for CERES on NPP. Edition 4 Aqua ADMs were used for flux

10   inversions for CERES-NPP measurements. However, the footprint size of CERES-NPP is

11   larger than that of CERES-Aqua, as the altitude of the NPP orbit is higher than that of the

12   Aqua orbit. Furthermore, cloud retrievals from VIIRS and MODIS, the imagers fly alongside

13   CERES-NPP and CERES-Aqua, are also different. To quantify the flux uncertainties due

14   to the footprint size difference between CERES-Aqua and CERES-NPP, and due to both

15   the footprint size difference and cloud property difference, a simulation is designed using

16   the MODIS pixel level data which are convolved with the CERES-Aqua and CERES-NPP

17   spectral response functions into their respective footprints. The simulation is designed to

18   isolate the effects of footprint size difference and cloud property difference on flux uncer-

19   tainty from calibration difference between CERES-NPP and CERES-Aqua. The footprint

20   size difference between CERES-Aqua and CERES-NPP introduces instantaneous flux un-

21   certainties in monthly gridded CERES-NPP of less than 4.0 $\mathrm{Wm^{-2}}$ for SW, and less than

22   1.0 $\mathrm{Wm^{-2}}$ for both daytime and nighttime LW. The global monthly mean instantaneous

23   SW flux from simulated CERES-NPP has a low bias of 0.4 $\mathrm{Wm^{-2}}$ and an uncertainty of

24   0.8 $\mathrm{Wm^{-2}}$, the LW has a bias of about 0.1 $\mathrm{Wm^{-2}}$ and an uncertainty of 0.2 $\mathrm{Wm^{-2}}$. These

25   uncertainties are within the uncertainties of CERES ADMs. When both footprint size and

26   cloud property differences are considered, the uncertainties of monthly gridded CERES-NPP

27   SW flux can be up to 20 $\mathrm{Wm^{-2}}$ in the Arctic regions where cloud optical depth retrievals

28   from VIIRS differ significantly from MODIS. The global monthly mean instantaneous SW

29   flux from simulated CERES-NPP has a high bias of 1.1 $\mathrm{Wm^{-2}}$ and an uncertainty of 2.4

30   $\mathrm{Wm^{-2}}$. LW flux shows less sensitivity to cloud property differences than SW flux, with the

31   uncertainties of about 2 $\mathrm{Wm^{-2}}$ in monthly gridded LW flux and about 0.3 $\mathrm{Wm^{-2}}$ for global

32   area-weighted monthly mean LW flux. These results highlight the importance of consistent

33 cloud retrieval algorithms to maintain the accuracy and stability of the CERES climate data

34 record.

1. Introduction

The Clouds and Earth's Radiant Energy System (CERES) project has been providing data products critical to advancing our understanding of the effects of clouds and aerosols on radiative energy within the Earth-atmosphere system. CERES data are used by the science community to study the Earth's energy balance (e.g., Trenberth et al. 2009; Kato et al. 2011; Loeb et al. 2012; Stephens et al. 2012), aerosol direct radiative effects (e.g., Satheesh and Ramanathan 2000; Zhang et al. 2005; Loeb and Manalo-Smith 2005; Su et al. 2013), aerosol-cloud interactions (Loeb and Schuster 2008; Quaas et al. 2008; Su et al. 2010b), and to evaluate global general circulation models (e.g., Pincus et al. 2008; Su et al. 2010a; Wang and Su 2013; Wild et al. 2013).

Six CERES instruments have flown on four different spacecrafts thus far. CERES pre-Flight Model (FM) on Tropical Rainfall Measuring Mission (TRMM) was launched on November 27, 1997 into a 350-km circular precessing orbit with a 35° inclination angle and flied together with the Visible and Infrared Scanner (VIRS). CERES instruments (FM1 and FM2) on Terra were launch on December 18, 1999 into a 705-km sun-synchronous orbit with a 10:30 a.m. equatorial crossing time. CERES instruments (FM3 and FM4) on Aqua spacecraft were launched on May 2, 2002 into a 705-km sun-synchronous orbit with a 1:30 p.m. equatorial crossing time. CERES on Terra and Aqua flies alongside Moderate-Resolution Imaging Spectroradiometer (MODIS). CERES FM5 instrument was launched onboard Suomi-NPP (hereafter referred to as NPP) on October 28, 2011 into a 824-km sun-synchronous orbit with a 1:30 p.m. equatorial crossing time and flies alongside the Visible Infrared Imaging Radiometer Suite (VIIRS). As the orbit altitudes differ among these space-crafts, the spatial resolutions of CERES instruments also vary from each other. TRMM has the lowest orbit altitude and offers the highest spatial resolution of CERES measurements, about 10 km at nadir; the spatial resolution of CERES on Terra and Aqua is about 20 km at nadir; and is about 24 km at nadir for NPP as it has the highest orbit altitude.

The CERES instrument consists of a three-channel broadband scanning radiometer (Wielicki

62 et al. 1996). The scanning radiometer measures radiances in shortwave (SW, 0.3-5 μm), win-

63 dow (WN, 8-12 μm), and total (0.3-200 μm) channels. The longwave (LW) component is

64 derived as the difference between total and SW channels. These measured radiances at

65 a given sun-Earth-satellite geometry are converted to outgoing reflected solar and emitted

66 thermal TOA radiative fluxes. To do so, the angular distribution of the radiance field must

67 be characterized for different scene types. Here scene type is a combination of variables

68 (e.g., surface type, cloud fraction, cloud optical depth, cloud phase, aerosol optical depth,

69 precipitable water, lapse rate, etc) that are used to group the data to develop distinct an-

70 gular distribution models (ADMs). To facilitate the construction of ADMs, there are pairs

71 of identical CERES instruments on both Terra and Aqua spacecrafts. At the beginning

72 of these missions one of the instruments on each spacecraft was always placed in a rotat-

73 ing azimuth plane (RAP) scan mode. In this mode, the instrument scans in elevation as

74 it rotates in azimuth, thus acquiring radiance measurements from a wide range of viewing

75 combinations. CERES instruments fly alongside high-resolution imagers, which provide ac-

76 curate scene type information within CERES footprints. Cloud and aerosol retrievals based

77 upon high-resolution imager measurements are averaged over CERES footprints by account-

78 ing for the CERES point spread function (PSF, Smith 1994) and are used for scene type

79 classification.

80 TRMM ADMs were developed using 9 months of CERES observations and the scene

81 identification information retrieved from VIRS observations (Loeb et al. 2003). Terra/Aqua

82 ADMs were developed using multi-year CERES measurements in RAP mode and in crosstrack

83 mode using the scene identification information from MODIS (Loeb et al. 2005; Su et al.

84 2015a). The high-resolution MODIS imager provides cloud conditions for every CERES foot-

85 print. The cloud algorithms developed by the CERES cloud working group retrieve cloud

86 fraction, cloud optical depth, cloud phase, cloud top and effective temperature/pressure

87 (among other variables) based on MODIS pixel-level measurements (Minnis et al. 2010).

88 These pixel-level cloud properties are spatially and temporally matched with the CERES

footprints and are used to select the scene-dependent ADMs to convert the CERES measured radiances to fluxes.

There is only one CERES instrument on NPP and it has been placed in cross-track scan mode since launch, it is thus not feasible to develop a specific set of ADMs for CERES on NPP. Currently, the Edition 4 Aqua ADMs (Su et al. 2015a) are used to invert fluxes for the CERES measurements on NPP. As mentioned earlier, the CERES footprint size on NPP is larger than that on Aqua. More importantly, the VIIRS channels are not identical to those of MODIS, especially the lack of water vapor (i.e. 6.7 μm) and CO2 channels, caused the cloud properties retrieved from MODIS and VIIRS differ from each other. ADMs are scene type dependent, it is important to use consistent scene identification for developing and applying the ADMs. Since the footprint sizes are different between CERES-Aqua and CERES-NPP, will using ADMs developed based on CERES-Aqua measurements for CERES-NPP flux inversion introduce any uncertainties in CERES-NPP flux? Additionally, as the cloud properties retrieved from VIIRS and MODIS differ from each other, the scene identification used to select the ADMs for flux inversion can also be different and thus lead to additional uncertainties in CERES-NPP flux. In this study, we design a simulation study to quantify the CERES-NPP flux uncertainties due to the footprint size difference alone, and due to both the footprint size and cloud property differences.

2. Method

We cannot answer the above questions by simply differencing the fluxes from CERES-Aqua and CERES-NPP, as the calibrations differ between these two CERES instruments and will be briefly discussed here. The Aqua and NPP orbits fly over each other about every 64 hours. These simultaneous observations from Aqua and NPP are matched to compare SW and LW radiances using CERES Aqua Edition 4 Single Scanner Footprint TOA/Surface Fluxes and Clouds (SSF) product and CERES NPP Edition 1 SSF product. The matching

criteria used for SW radiances are that the latitude and longitude differences between the Aqua footprints and the NPP footprints are less than 0.05 degree, solar zenith angle difference is less than 2 degrees, viewing zenith angle and relative azimuth angle differences are less than 5 degrees. Same latitude and longitude matching criteria are used for LW radiances and the viewing zenith angle difference between the Aqua footprints and the NPP footprints is less than 2 degrees. Figure 1 shows the SW, daytime LW, and nighttime LW radiance comparisons between CERES-Aqua and CERES-NPP using matched footprints of 2013 and 2014. The total number of matched footprints, the mean radiances from CERES-Aqua and CERES-NPP, and the root-mean-square errors are summarized in Table 1. The mean SW radiance measured by CERES-NPP is about 1 $Wm^{-2}sr^{-1}$ higher than that measured by CERES-Aqua, the daytime mean LW radiance from CERES-NPP is about 0.4 $Wm^{-2}sr^{-1}$ lower than that from CERES-Aqua, and the nighttime LW radiance agrees to within 0.1 $Wm^{-2}sr^{-1}$. These differences do not show any view zenith angle dependence. The daytime LW radiance is derived as the difference between total channel and SW channel measurements, and the nighttime LW radiance is simply from the total channel measurements. The differences shown in Table 1 indicate that the calibration of total channels between CERES-Aqua and CERES-NPP agrees very well, and the difference in SW channel calibration could be the cause for the relatively larger daytime LW differences. More research is needed to understand the calibration differences between CERES-Aqua and CERES-NPP.

To quantify the footprint size and cloud retrieval effect on flux inversion without having to account for the calibration differences, we design a simulation study using the MODIS pixel level data. Figure 2 illustrates the process of generating the simulated footprints from the MODIS pixels (represented by the small squares). These pixel-level spectral measurements are used to retrieve cloud properties and aerosol optical depth. These pixel-level imager-derived aerosol and cloud properties, and spectral radiances from MODIS are convolved with the CERES PSF to provide the most accurate aerosol and cloud properties that are spatially and temporally matched with the CERES broadband radiance data. We first

use the CERES-Aqua PSF to convolve the aerosol/cloud properties, and the spectral radi-

ances (and other ancillary data) into Aqua-size footprints (orange ovals of the top figure),

as is done for the standard CERES-Aqua SSF product. We then increase the footprint size

to be that of NPP (orange ovals of the bottom figure) and use the CERES-NPP PSF to

average cloud/aerosol properties, spectral radiances, and other ancillary data into the sim-

ulated NPP footprints. Four months (July 2012, October 2012, January 2013, and April

2013) of simulated CERES-Aqua and CERES-NPP data were created. For every CERES-

Aqua footprint, it contains the broadband SW and LW radiances measured by the CERES

instrument. The simulated NPP footprints however do not contain broadband radiances.

To circumvent this issue, we developed narrowband-to-broadband coefficients to convert the

MODIS spectral radiances to broadband radiances.

The Edition 4 CERES-Aqua SSF data from July 2002 to September 2007 are used to

derive the narrowband-to-broadband regression coefficients separately for SW, daytime LW,

and nighttime LW. Seven MODIS spectral bands (0.47, 0.55, 0.65, 0.86, 1.24, 2.13, and 3.7

μm) are used to derive the broadband SW radiances, and the SW regression coefficients are

calculated for every calendar month for discrete intervals of solar zenith angle, viewing zenith

angle, relative azimuth angle, surface type, snow/non-snow conditions, cloud fraction, and

cloud optical depth. Five MODIS spectral bands (6.7, 8.5, 11.0, 12.0, and 14.2 μm) are used

to derived the broadband LW radiances, and the LW regression coefficients are calculated

for every calendar month for discrete intervals of viewing zenith angle, precipitable water,

surface type, snow/none-snow conditions, cloud fraction, and cloud optical depth. The 20

International Geosphere-Biosphere Programme (IGBP) surface types are grouped into 8

surface types: ocean, forest, savanna, grassland, dark desert, bright desert, the Greenland

permanent snow, and the Antarctic permanent snow. When there is sea ice over the ocean

and snow over the land surface types, regression coefficients for ice and snow conditions are

developed (only footprints with 100% sea ice/snow coverage are considered).

These SW and LW narrowband-to-broadband regression coefficients are then applied to

the spectral radiances in each simulated CERES-Aqua and simulated CERES-NPP foot-print, if the footprint consists of a single surface type. Even though the CERES-Aqua footprints contained the broadband radiances from CERES observations, we choose to use the broadband radiances calculated using the narrowband-to-broadband regressions to en-sure that the broadband radiances are consistent between the simulated CERES-Aqua and the simulated CERES-NPP. Doing so we can isolate the flux difference between simulated CERES-Aqua and simulated CERES-NPP caused solely by footprint size difference. These broadband radiances derived using the narrowband-to-broadband coefficients are then con-verted to fluxes using the cloud properties retrieved from MODIS observations and the Aqua ADMs. As the footprint sizes are different between CERES-Aqua and CERES-NPP, flux differences cannot be assessed on the footprint level, monthly grid box (1° latitude by 1° longitude) mean flux differences are used to assess the CERES-NPP gridded instantaneous flux uncertainties. These monthly gridded instantaneous flux differences and the absolute flux differences are then area-weighted to provide the global monthly mean instantaneous flux bias and uncertainty.

3. Results

The monthly mean instantaneous TOA SW fluxes derived using the regression generated broadband radiances for simulated CERES-Aqua are shown in Figure 3(a) for April 2013. Note these fluxes are different from those in the Edition 4 Aqua SSF product as the CERES measured radiances differ from those inferred using narrowband-to-broadband regression coefficients. The flux differences caused by the footprint size difference between the simulated CERES-Aqua and the simulated CERES-NPP are shown in Figure 3(b). Grid boxes in white indicate that the number of footprints with valid SW fluxes differ by more than 2% between simulated CERES-Aqua and CERES-NPP, as the narrowband-to-broadband regressions are only applied to footprints that consist with the same surface types which result in less

footprints with valid fluxes for CERES-NPP than for CERES-Aqua. The footprint size difference between CERES-Aqua and CERES-NPP introduces an uncertainty that rarely exceeds 4.0 Wm^{-2} in monthly gridded CERES-NPP instantaneous SW fluxes. For global monthly mean instantaneous SW flux, the simulated CERES-NPP has a low bias of 0.4 Wm^{-2} and an uncertainty of 0.8 Wm^{-2}. Results from the other three months are very similar to April 2013 (not shown).

The cloud properties in the simulated CERES-Aqua footprints and in the simulated CERES-NPP footprints are all based upon MODIS retrievals, so the scene identifications used to select ADMs for flux inversion are almost the same for both the CERES-Aqua and the CERES-NPP, except small differences due to differing footprint sizes. However, the cloud properties retrieved using MODIS and VIIRS are different, especially over the polar regions. Figure 4 shows the daytime cloud fraction and cloud optical depth difference between VIIRS and Aqua-MODIS for April 2013. VIIRS retrieval of cloud fraction is greater than that from MODIS by up to 10% and the VIIRS retrieval of cloud optical depth is smaller than that from MODIS by 2∼3 over part of the Antarctic. VIIRS retrieval of cloud fraction over the northern high-latitude snow regions is smaller than that from MODIS, while the optical depth from VIIRS is higher than that from MODIS. Over the Arctic, cloud optical depth from VIIRS is much higher than that from MODIS. Over the ocean from 60°S to 60°N, the differences in cloud fraction seem rather random while the differences in cloud optical depth is mostly positive (VIIRS retrieval is higher than Aqua-MODIS retrieval). Polar region cloud fraction differences are mainly because that VIIRS lacks the water vapor and CO2 channels which affect the polar cloud mask algorithm. VIIRS retrieval also use different parameterization of 1.24 μm reflectance which affects cloud optical depth retrieval over the snow/ice surfaces.

These cloud retrieval differences affect the anisotropy factors selected for flux inversion. The cloud fraction and cloud optical depth retrievals from MODIS convolved in the simulated CERES-NPP footprints are adjusted to be similar to those from VIIRS retrievals to assess

how cloud retrieval differences affect the flux. To accomplish this, daily cloud fraction ratios of VIIRS to MODIS are calculated for each 1° latitude by 1° longitude grid box. These ratios are then applied to the cloudy footprints of MODIS retrieval to nudge the MODIS cloud fractions to be nearly the same as those from VIIRS retrieval. Note no adjustment is done for clear footprints. Similarly, daily cloud optical depth ratios of VIIRS to MODIS are calculated using cloudy footprints for each 1° by 1° grid box. These ratios are used to adjust the MODIS retrieved cloud optical depth to be close to those from VIIRS retrievals.

Figure 3(c) shows the SW flux difference caused by both the footprint size and cloud property differences. Adding the cloud property differences increase the CERES-NPP flux uncertainty compared to when only footprint size differences are considered (Figure 3(b)), regional instantaneous flux uncertainty over the Arctic ocean can exceed 20 Wm^{-2}. Accounting for cloud property differences, the global mean instantaneous SW flux from simulated CERES-NPP has a high bias of 1.1 Wm^{-2} and the uncertainty is increased to 2.4 Wm^{-2}. Over the Arctic Ocean, the cloud optical depth from VIIRS retrieval is much higher than that from the MODIS retrieval while the difference in cloud fraction is relatively small. The polar regions are dominated by oblique views and the anisotropy factors for thick clouds are smaller than those for thin clouds at these oblique angles, which led to large flux increase when using VIIRS cloud properties for flux inversion.

The daytime and nighttime instantaneous LW flux from the simulated CERES-Aqua footprints, LW flux differences due to footprint size difference, and LW flux difference due to both footprint size difference and cloud property difference are shown in Figures 5 and 6. The effect of footprint size on instantaneous LW flux uncertainty is generally within 1.0 Wm^{-2} for gridded monthly mean LW flux, and the uncertainty of global monthly mean LW flux is within 0.2 Wm^{-2}. When cloud property differences are also considered, the uncertainty of monthly gridded LW fluxes increases to about 2 Wm^{-2} with the uncertainty of global monthly mean LW flux of about 0.3 Wm^{-2}. The instantaneous LW fluxes showed much less sensitivity to cloud property changes than the SW fluxes, especially over the Arctic Ocean

247 where cloud optical depth changed significantly. This is because the LW ADMs over the

248 snow/ice surfaces have very little sensitivity to cloud optical depth (Su et al. 2015a), but

249 they were developed for discrete cloud fraction intervals and larger flux changes are noted

250 in regions experiencing large cloud fraction changes.

4. Summary and discussion

252   The scene-type dependent ADMs are used to convert the radiances measured by the

253 CERES instruments to fluxes. Specific empirical ADMs were developed for CERES instru-

254 ments on TRMM, Terra, and Aqua (Loeb et al. 2003, 2005; Su et al. 2015a). As there is only

255 one CERES instrument on NPP and it has being placed in cross track mode since launch, it is

256 not possible to construct a set of ADMs specific for CERES on NPP. Edition 4 Aqua ADMs

257 (Su et al. 2015a) are thus used for flux inversions for CERES-NPP measurements. However,

258 the altitude of the NPP orbit is higher than that of the Aqua orbit resulting in a larger

259 CERES footprint size on NPP than on Aqua. Given that the footprint size of CERES-NPP

260 is different from that of CERES-Aqua, we need to quantify the CERES-NPP flux uncer-

261 tainty caused by using the CERES-Aqua ADMs. Furthermore, there are some differences

262 between the imagers fly alongside CERES-Aqua (MODIS) and CERES-NPP (VIIRS), as

263 VIIRS lacks the water vapor and CO_2 channels. These spectral differences and algorithm

264 differences lead to notable cloud property differences retrieved from MODIS and VIIRS.

265 As the anisotropy factors are scene-type dependent, differences in cloud properties will also

266 introduce uncertainties in flux inversion.

267   To quantify the flux uncertainties due to the footprint size difference between CERES-

268 Aqua and CERES-NPP, and due to both the footprint size difference and cloud property

269 difference, we use the MODIS pixel level data to simulate the CERES-Aqua and CERES-

270 NPP footprints. The simulation is designed to isolate the effects of footprint size differ-

271 ence and cloud property difference on flux uncertainty from calibration difference between

CERES-NPP and CERES-Aqua. Comparisons using two years of collocated CERES-Aqua and CERES-NPP footprints indicate that the SW radiances from CERES-NPP is about 1.5% higher than those from CERES-Aqua, the daytime LW radiance from CERES-NPP is about 0.5% lower than those from CERES-Aqua, and the nighttime LW radiances agree to within 0.1%. The pixel-level MODIS spectral radiances, the imager-derived aerosol and cloud properties, and other ancillary data are first convolved with the CERES Aqua PSF to generate the simulated CERES-Aqua footprints, and then convolved with the CERES NPP PSF to generate the simulated CERES-NPP footprints. Broadband radiances within the simulated CERES-Aqua and CERES-NPP footprints are derived using the MODIS spectral bands based upon narrowband-to-broadband regression coefficients developed using five-years of Aqua data, thus ensure consistency between broadband radiances from simulated CERES-Aqua and CERES-NPP. These radiances are then converted to fluxes using the CERES-Aqua ADMs. The footprint size difference between CERES-Aqua and CERES-NPP introduces instantaneous flux uncertainties in monthly gridded CERES-NPP of less than 4.0 Wm^{-2} for SW, and less than 1.0 Wm^{-2} for both daytime and nighttime LW. Area-weighted monthly gridded instantaneous flux differences and the absolute flux differences are used to quantify the global monthly mean instantaneous flux bias and uncertainty. The global monthly mean instantaneous SW flux from simulated CERES-NPP has a low bias of 0.4 Wm^{-2} and an uncertainty of 0.8 Wm^{-2}, the LW has a bias of about 0.1 Wm^{-2} and an uncertainty of 0.2 Wm^{-2}.

The cloud properties in the simulated CERES-Aqua footprints and in the simulated CERES-NPP footprints are all based upon MODIS retrievals, but in reality cloud properties retrieved from VIIRS differ from those from MODIS. To assess the flux uncertainty from scene identification differences, cloud fraction and cloud optical depth in the simulated CERES-NPP footprints are perturbed to be more like the VIIRS retrievals. When both footprint size and cloud property differences are considered, the uncertainties of monthly gridded CERES-NPP SW flux can be up to 20 Wm^{-2} in the Arctic regions where cloud

optical depth retrievals from VIIRS differ significantly from MODIS. The global monthly mean instantaneous SW flux from simulated CERES-NPP has a high bias of 1.1 Wm^{-2} and an uncertainty of 2.4 Wm^{-2}. LW flux shows less sensitivity to cloud property differences than SW flux, with the uncertainties of about 2.0 Wm^{-2} in monthly gridded LW flux and about 0.3 Wm^{-2} for global area-weighted monthly mean LW flux.

This simulation study indicates that the footprint size differences between CERES-NPP and CERES-Aqua introduce flux differences that are within the uncertainties of CERES ADMs (Su et al. 2015b). However, the uncertainty assessment provided here should be considered as the low end, as many regions (especially over land, snow, and ice) were not included due to sample number differences within the grid boxes. When cloud property differences are accounted for, the SW flux uncertainties increase significantly and exceed the uncertainties of CERES ADMs. These findings indicate that inverting CERES-NPP flux using CERES-Aqua ADMs resulting in flux uncertainties that are within the ADMs uncertainties as long as the cloud retrievals between VIIRS and MODIS are consistent. When the cloud retrieval differences between VIIRS and MODIS are accounted, the SW flux uncertainties exceed the ADM uncertainties. To maintain the consistency of the CERES climate data record, it is thus important to maintain the consistency of cloud retrieval algorithms.

Acknowledgments.

This research has been supported by the NASA CERES project. The authors thank Norman Loeb and Patrick Minnis for helpful discussions.

321

REFERENCES

322

323 Kato, S., et al., 2011: Improvements of top-of-atmosphere and surface irradiance computa-

324 tion with CALIPSO-, and MODIS-derived cloud and aerosol properties. *J. Geophys. Res.*,

325 **116 (D19209)**, D19 209, doi:10.1029/2011JD016050.

326 Loeb, N. G., S. Kato, K. Loukachine, and N. Manalo-Smith, 2005: Angular distribution

327 models for top-of-atmosphere radiative flux estimation from the clouds and the earth's

328 radiant energy system instrument on the terra satellite. part I: Methodology. *J. Atmos.*

329 *Oceanic Technol.*, **22**, 338–351.

330 Loeb, N. G., J. M. Lyman, G. C. Johnson, R. P. Allan, D. R. Doelling, T. Wong, B. J.

331 Soden, and G. L. Stephens, 2012: Observed changes in top-of-the-atmosphere radiation

332 and upper-ocean heating consistent within uncertainty. *Nature Geosci.*, **5**, 110–113, doi:

333 10.1038/NGEO1375.

334 Loeb, N. G. and N. Manalo-Smith, 2005: Top-of-atmosphere direct radiative effect of aerosols

335 over global oceans from merged CERES and MODIS observations. *J. Climate*, **18**, 3506–

336 3526.

337 Loeb, N. G., N. Manalo-Smith, S. Kato, W. F. Miller, S. K. Gupta, P. Minnis, and B. A.

338 Wielicki, 2003: Angular distribution models for top-of-atmosphere radiative flux estima-

339 tion from the Clouds and the Earth's Radiant Energy System instrument on the Tropical

340 Rainfall Measuring Mission satellite. Part I: Methodology. *J. Appl. Meteor.*, **42**, 240–265.

341 Loeb, N. G. and G. L. Schuster, 2008: An observational study of the relationship between

342 cloud, aerosol and meteorology in broken low-level cloud conditions. *J. Geophys. Res.*,

343 **113 (D14214)**, D14 214, doi:10.1029/2007JD009763.

344 Minnis, P., et al., 2010: CERES Edition 3 cloud retrievals. *13th Conference on Atmospheric*

345 *Radiation*, Am. Meteorol. Soc., Oregon, Portland.

346 Pincus, R., C. P. Batstone, R. J. P. Hofmann, K. E. Taylor, and P. J. Glecker, 2008: Evalu-

347 ating the present-day simulation of clouds, precipitation, and radiation in climate models.

348 *J. Geophys. Res.*, **113 (D14209)**, D14 209, doi:10.1029/2007JD009334.

349 Quaas, J., O. Boucher, N. Bellouin, and S. Kinne, 2008: Satellite-based estimate of the

350 direct and indirect aerosol climate forcing. *J. Geophys. Res.*, **113 (D05204)**, D05 204,

351 doi:10.1029/2007JD008962.

352 Satheesh, S. K. and V. Ramanathan, 2000: Large differences in tropcial aerosol forcing at

353 the top of the atmosphere and earth's surface. *Nature*, **405**, 60–63.

354 Smith, G. L., 1994: Effects of time response on the point spread function of a scanning

355 radiometer. *Appl. Opt.*, **33**, 7031–7037.

356 Stephens, G. L., et al., 2012: An update on Earth's energy balance in light of the latest

357 global observations. *Nature Geosci.*, **5**, 691–696, doi:10:1038/NGEO1580.

358 Su, W., A. Bodas-Salcedo, K.-M. Xu, and T. P. Charlock, 2010a: Comparison of the trop-

359 ical radiative flux and cloud radiative effect profiles in a climate model with Clouds and

360 the Earth's Radiant Energy System (CERES) data. *J. Geophys. Res.*, **115 (D01105)**,

361 D01 105, doi:10.1029/2009JD012490.

362 Su, W., J. Corbett, Z. A. Eitzen, and L. Liang, 2015a: Next-generation angular distribution

363 models for top-of-atmosphere radiative flux calculation from the CERES instruments:

364 Methodology. *Atmos. Meas. Tech.*, **8**, 611–632, doi:10.5194/amt-8-611-2015.

365 Su, W., J. Corbett, Z. A. Eitzen, and L. Liang, 2015b: Next-generation angular distribution

366 models for top-of-atmosphere radiative flux calculation from the CERES instruments:

367 Validation. *Atmos. Meas. Tech.*, **8**, 3297–3313, doi:10.5194/amt-8-3297-2015.

Su, W., N. G. Loeb, G. L. Schuster, M. Chin, and F. G. Rose, 2013: Global all-sky shortwave direct radiative forcing of anthropogenic aerosols from combined satellite observations and GOCART simulations. *J. Geophys. Res.*, **118**, 1–15, doi:10.1029/2012JD018294.

Su, W., N. G. Loeb, K. Xu, G. L. Schuster, and Z. A. Eitzen, 2010b: An estimate of aerosol indirect effect from satellite measurements with concurrent meteorological analysis. *J. Geophys. Res.*, **115 (D18219)**, D18 219, doi:10.1029/2010JD013948.

Trenberth, K. E., J. T. Fasullo, and J. Kiehl, 2009: Earth's global energy budget. *Bull. Am. Meteor. Soc.*, **90**, 311–323, doi:10.1175/2008BAMS2634.1.

Wang, H. and W. Su, 2013: Evaluating and understanding top of the atmosphere cloud radiative effects in Intergovernmental Panel on Climate Change (IPCC) fifth assessment report (AR5) cloupled model intercomparison project phase 5 (CMIP5) models using satellite observations. *J. Geophys. Res.*, **118**, 1–17, doi:10.1029/2012JD018619.

Wielicki, B. A., B. R. Barkstrom, E. F. Harrison, R. B. Lee, G. L. Smith, and J. E. Cooper, 1996: Clouds and the Earth's Radiant Energy System (CERES): An Earth Observing System experiment. *Bull. Amer. Meteor. Soc.*, **77**, 853–868.

Wild, M., D. Folini, C. Schar, N. G. Loeb, E. G. Dutton, and G. Konig-Langlo, 2013: The global energy balance from a surface perspective. *Clim. Dyn.*, **40**, 3107–3134, doi: 10.1007/s00382-012-1569-8.

Zhang, J., S. A. Christopher, L. A. Remer, and Y. J. Kaufman, 2005: Shortwave aerosol radiative forcing over cloud-free oceans from Terra: 2. Seasonal and global distributions. *J. Geophys. Res.*, **110 (D10S24)**, D10S24, doi:10.1029/2004JD005009.

List of Tables

TABLE 1. Comparison of SW, daytime LW, and nighttime LW radiances (Wm^{-2}sr^{-1}) between CERES-Aqua and CERES-NPP using matched footprints of 2013 and 2014.

	SW	Daytime LW	Nighttime LW
Sample Number	363203	192178	187880
Mean CERES-Aqua Radiance	69.2	77.4	74.4
Mean CERES-NPP Radiance	70.2	77.0	74.3
RMS Error	4.4	1.6	0.8

List of Figures

FIG. 1. Radiance comparisons between matched CERES-Aqua and CERES-NPP footprints,
(a) SW; (b) daytime LW; and (c) nighttime LW using data of 2013 and 2014.
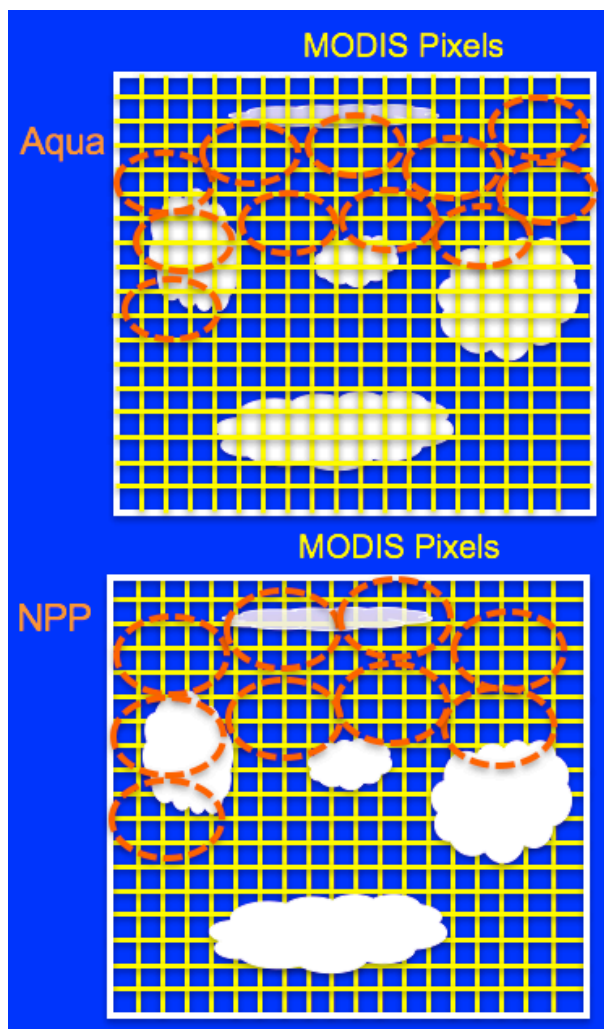
Fig. 2. Scheme of convoluting the MODIS pixels into the Aqua and NPP footprints.
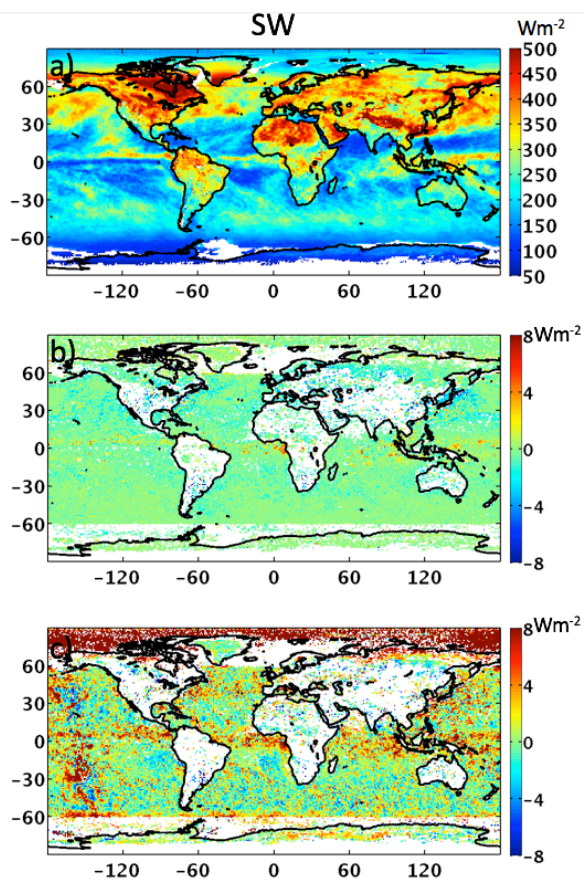
FIG. 3. The monthly gridded mean TOA instantaneous SW fluxes derived based upon the broadband radiances from regression coefficients for the Aqua footprints (a), the flux differences caused by footprint size difference between simulated NPP and Aqua (b), and the flux differences caused by both footprint size and cloud property differences (c) using April 2013 data. Regions shown in white have large sample number differences between Aqua and simulated NPP.
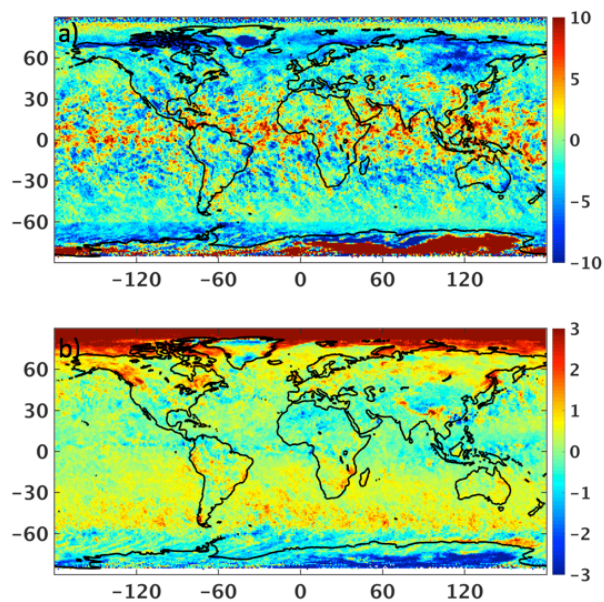
FIG. 4. Cloud fraction (a) and cloud optical depth (b) differences between VIIRS and MODIS retrievals for April 2013.
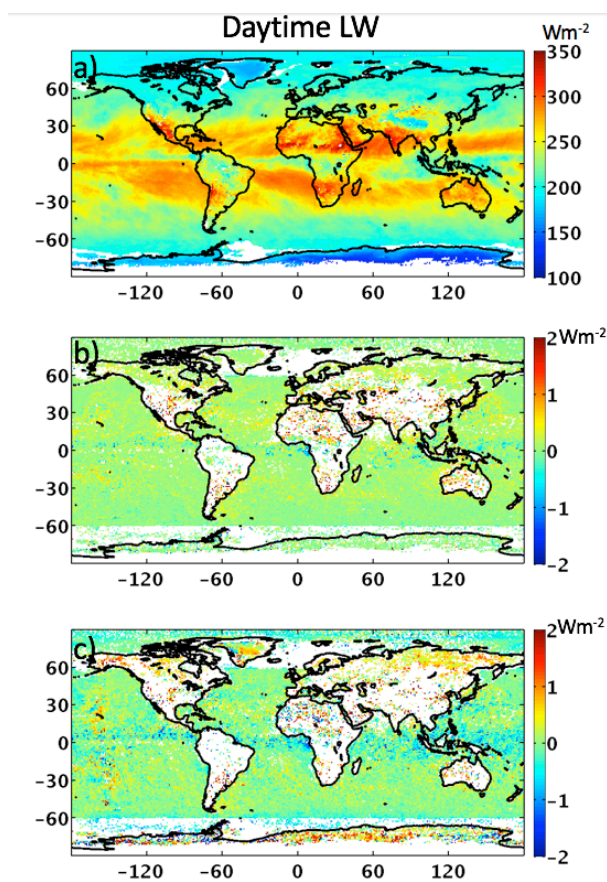
FIG. 5. The monthly gridded mean TOA daytime LW fluxes derived based upon the broadband radiances from regression coefficients for the Aqua footprints (a), the flux differences caused by footprint size difference between simulated NPP and Aqua (b), and the flux differences caused by both footprint size and cloud property differences (c) using April 2013 data. Regions shown in white have large sample number differences between Aqua and simulated NPP.
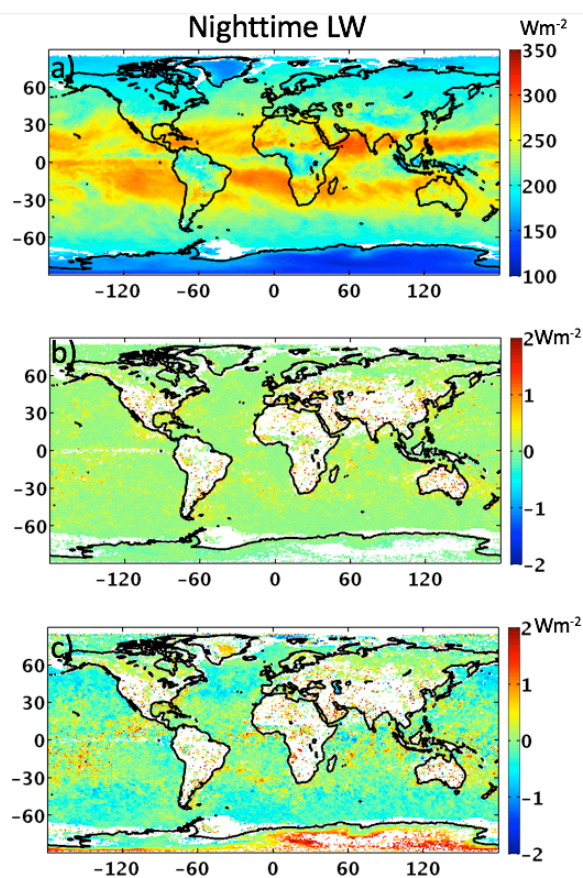
Fig. 6. The monthly gridded mean TOA nighttime LW fluxes derived based upon the broadband radiances from regression coefficients for the Aqua footprints (a), the flux differences caused by footprint size difference between simulated NPP and Aqua (b), and the flux differences caused by both footprint size and cloud property differences (c) using April 2013 data. Regions shown in white have large sample number differences between Aqua and simulated NPP.